U.S. Department
of Transportation
**National Highway
Traffic Safety
Administration**

NHTSA

DOT HS 812 810

January 2020

Battery State of Health and Stability Diagnostic Tool Set Development

DISCLAIMER

Suggested APA Format Citation:

Lamb, J., Torres-Castro, L., Tanim, T., Dufek, E., Ho, C., & Walker, L. (2020, January). *Battery state of health and stability diagnostic tool set development* (Report No. DOT HS 812 810). Washington, DC: National Highway Traffic Safety Administration.

1. Report No. DOT HS 812 810	2. Government Accession No.	3. Recipient's Catalog No.
4. Title and Subtitle Battery State of Health and Stability Diagnostic Tool Set Development		5. Report Date January 2020 6. Performing Organization Code
7. Authors Joshua Lamb, Loraine Torres-Castro, Tanvir Tanim, Eric Dufek, Chinh Ho, and Lee Walker		8. Performing Organization Report No.
9. Performing Organization Name and Address Sandia National Laboratories P.O. Box 5800 Albuquerque, NM 87185 and Idaho National Laboratory 2525 Fremont Avenue Idaho Falls, ID 83402		10. Work Unit No. (TRAIS) 11. Contract or Grant No.
12. Sponsoring Agency Name and Address National Highway Traffic Safety Administration 1200 New Jersey Avenue SE Washington, DC 20590		13. Type of Report and Period Covered Final Report 14. Sponsoring Agency Code

15. Supplementary Notes

Acknowledgements: Sandia National Laboratories is a multimission laboratory managed and operated by National Technology & Engineering Solutions of Sandia, LLC, a wholly owned subsidiary of Honeywell International Inc., for the U.S. Department of Energy's National Nuclear Security Administration under contract DE-NA0003525. The Idaho National Laboratory is a U.S. Department of Energy National Laboratory operated by Battelle Energy Alliance, LLC, under contract No. AC07-05ID14517.

16. Abstract

Traditional monitoring of electrochemical cells and batteries has been limited to voltage and sometimes temperature of the cell or cells. There are limits to how predictive voltage and temperature can be prior to thermal runaway events. They are often lagging indicators of battery failure, and by the time a noticeable change is detected it is too late to arrest cell failure with intervention or maintenance. Furthermore, instantaneous voltage and temperature monitoring are often inadequate to determine the state of a battery at rest, particularly if the battery has been subjected to an abusive condition. Knowledge of the stability of a damaged battery would allow for both safer and more efficient handling. This work examines the application of rapid electrochemical impedance spectroscopy (EIS) as a tool to determine stability of an electrochemical cell or battery to provide deeper understanding of how abused cells and batteries fail, and the technical basis of a tool that could be used to interrogate and even monitor cells for early signs of damage or failure. These tests looked for markers within the EIS data that correspond to the onset of unstable conditions. The primary drawback of traditional EIS is typically the time involved to take a full measurement, which limited impedance measurements to either full spectra of stable systems, or dynamic measurements at a single high frequency, such as 1 kHz. Further, single-frequency measurements generally only yield limited information. Fast-impedance techniques have been developed but typically require expensive hardware and sophisticated data analysis to replicate the data obtained through traditional measurements. Idaho National Laboratories has developed a fast-impedance tool that uses off-the-shelf parts. This work evaluated that rapid impedance tool, including replicating the work performed with the traditional tool as well as collecting impedance data during dynamic conditions.

17. Key Words	18. Distribution Statement
electrochemical impedance spectroscopy, EIS, battery failure, cell failure, rapid impedance, thermal runaway	No restrictions. This document is available to the public through the National Technical Information Service, www.ntis.gov.

19. Security Classif. (of this report)	20. Security Classif. (of this page)	21. No. of Pages	22. Price
Unclassified	Unclassified	33	

Form DOT F 1700.7 (8-72) **Reproduction of completed page authorized**

TABLE OF CONTENTS

NOMENCLATURE

BMS	Battery Management System
DOE	Department of Energy
EIS	Electrochemical impedance spectroscopy
LFP	Lithium Iron Phosphate cathode
NMC	Nickel Manganese Cobalt Oxide (LiNixMnyCozO2) cathode
SNL	Sandia National Laboratories
SOC	State of charge
SOH	State of health
SOF	State of functionality
IMB	Impedance measurement box
INL	Idaho National Laboratory

INTRODUCTION

Traditional monitoring of electrochemical cells and batteries has been limited to observation of voltage and sometimes temperature of the cell or cells. While this monitoring can be very robust, there are limits to how predictive voltage and temperature behavior can be prior to a thermal runaway event. Ultimately, voltage and temperature changes are often lagging indicators of battery failure, and by the time a noticeable change is detected it is too late to arrest cell failure with intervention or maintenance. Furthermore, instantaneous voltage and temperature monitoring are often inadequate to determine the state of a battery at rest, particularly if the battery has been previously subjected to an abusive condition. Proper handling of a battery after an abusive event generally requires assuming the battery is potentially unstable and may yet undergo a thermal runaway event. This usually requires full discharge and/or destruction of the battery after an abusive event whether a thermal runaway was observed or not. Knowledge of the level of stability of a damaged battery would allow for both safer and more efficient handling of the abused battery.

This work examines the application of rapid electrochemical impedance spectroscopy (EIS) as a tool for determining the state of stability of an electrochemical cell or battery. The cells for this study were subjected to thermal and electrical abuse coupled with EIS monitoring at differing levels of battery abuse. This aims to not only provide a deeper understanding of how abused cells and batteries fail, but also form the technical basis of a tool that could ultimately be used to interrogate cells of unknown stability and even monitor active cells for early signs of damage or failure. These tests looked for markers within the EIS data that correspond to the onset of unstable conditions. These markers can be potentially applied to interrogate batteries of an unknown stability as well as provide the basis for an active diagnostic method as part of a battery management system.

The primary drawback of traditional EIS is that it is typically not suited for measurements of dynamic systems due to the time involved to take a full measurement. This has historically limited the use of impedance measurements to either full spectra of stable systems, or dynamic measurements at a single high frequency, such as 1 kHz. These have significant drawbacks, as limiting the measurement to stable systems would preclude its use as an on-board diagnostics tool. Further, single-frequency measurements generally only yield limited information. Fast-impedance techniques have been developed previously, but typically require expensive hardware and sophisticated data analysis to replicate the data obtained through traditional measurements. Idaho National Laboratories (INL) has developed a fast-impedance tool that uses off the shelf parts. This work evaluated the rapid impedance tool, including both replicating the work performed with the traditional tool as well as collecting impedance data during dynamic conditions.

EXPERIMENTAL METHODS

Testing was focused on large format cells of NMC and LFP cathode chemistries as well as work with more complex modules. Aging and external short circuit studies were performed using 16 Ah Kokam NMC-graphite cells. Abuse testing was performed on 10 Ah NMC-graphite and LFP-graphite cells manufactured by AA Portable Power Corp. Cells were obtained through commercial-off-the-shelf (COTS) sources.

Cell Aging

To understand the impact that different aged cells had on impedance response, a set of cells was aged at 55^0C using a cycling profile between the minimum and maximum voltage at a C/1 rate. NMC-graphite cells were aged to roughly 29 percent fade from their initial, experimentally determined capacity of 1.25 Ah. Following aging cells were discharged to their minimum voltage and held at that voltage until a C/100 current (0.012 A) was obtained to ease string configuration.

Testing with the INL fast-impedance measurement tool

Rapid acquisition of impedance data was performed using a rapid impedance measurement tool first developed at INL. The impedance measurement box (IMB) measurements were for frequencies ranging from 0.1 to 1638 Hz. The IMB used was of the third generation of the tool and had a maximum operating window of 50V.

For no load measurements, the string was charged to a set voltage for each SOC level as determined from a single cell open circuit voltage (OCV) versus SOC diagram. The cell was then put into a rest state and the impedance data was acquired followed by further charging or discharging of the cell. For all charge measurements, the SOC was collected in a consecutively increasing manner and for the discharge measurements the SOC was consecutively decreasing.

For under-load conditions where an active charge/discharge current was applied the measurements were started when the appropriate voltage from the SOC diagram was reached. During the measurement the load on the string was maintained. As with the no load measurements the data was acquired with an increasing SOC for charging events and a decreasing SOC for discharge measurements.

RESULTS

Battery state of stability evaluation under major abuse scenarios at SNL

Work in this phase has focused on establishing the impacts of partial abuse, as well as the ability of diagnostic techniques studied to identify failures in battery packs of increasing capacity and complexity. This has included increasing the number of cells and using increasingly complex series/parallel combinations of cells. Much of this work has also focused on NMC and LFP cathode chemistries, both to provide a broad base of knowledge of the functionality of the techniques in comparison to LCO cathodes previously studied, and to focus on chemistries relevant to large battery systems.

Figures 1 to 5 show the results of applying varying levels of overcharge to 10 Ah NMC/graphite cells while **Figure 6** illustrates the application of the diagnostic technique to complex battery packs. **Figure 1** shows the temperature and voltage profiles of the cell as a function of state of charge. Notably in this data, there is little temperature rise until ~135 percent state of charge, with a slow, steady increase in the voltage as the SOC rises. While this is easily observable when making detailed measurements of a single cell, there are always limitations to voltage and temperature monitoring in large packs and these key indicators may be missed.

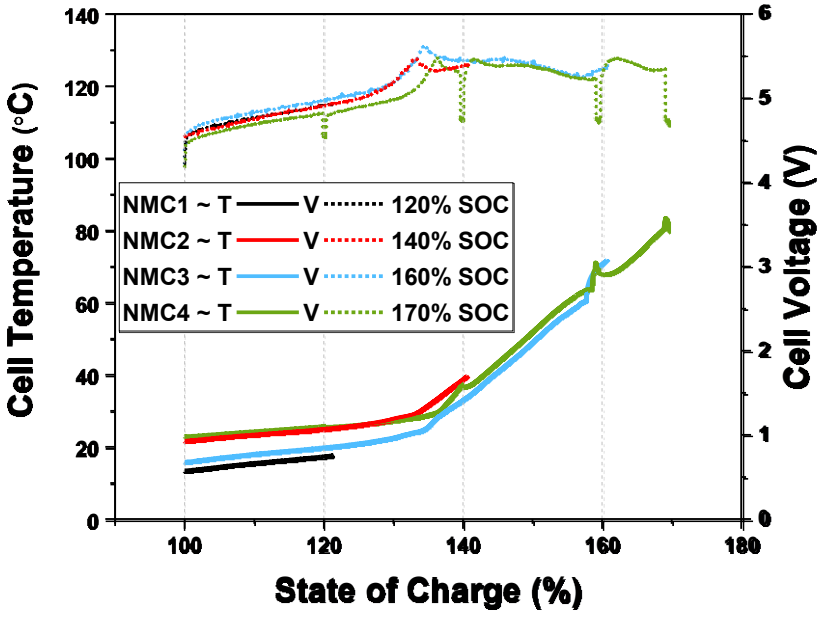

Figure 1: Voltage and temperature curves collected during in-operando testing of NMC cathode cells.

Figure 2 shows the complex impedance results of measurements taken during the overcharge of the cells up to and reported at various levels of state of charge. **Figure 3** shows the impact to the scalar impedance with increasing overcharge at various target frequencies, and **Figure 4** shows further analysis of the complex data based on equivalent circuit modeling of the complex impedance data in **Figure 2d**. The data for all the cells showed a distinct transition that occurs from 120 percent to 140 percent total SOC, particularly at low frequencies. This translates well to processes within the equivalent circuit that are active at low frequencies like the charge transfer resistance (R_{CT}).

The changes in the scalar impedance in **Figure 3** are particularly useful from a diagnostic standpoint, as this provides an easily tracked value that could serve as a potential alarm bell if the impedance was observed to rise suddenly. This would potentially allow for some single-frequency monitoring, but does suggest that the most useful frequencies are on the lower end. Here we see the largest impact a 0.1 Hz, where a single-frequency measurement would take 10 seconds. This also identifies a target range for a potential physical transition within the chemistry that occurs between 120 and 140 percent total SOC. This, coupled with the abuse data, points to

a transition point when the battery goes from suffering standard performance degradation due to wear to displaying damage with alarming symptoms of instability.

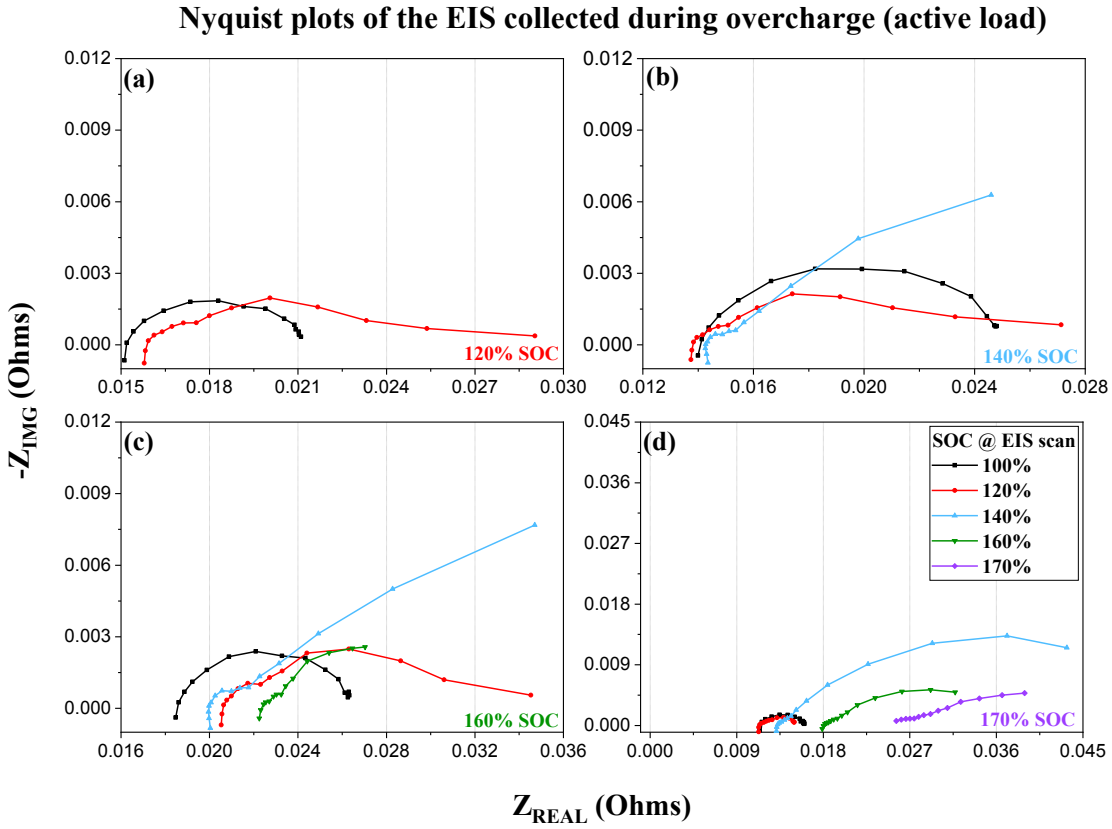

Figure 2: NMC In-operando impedance results.

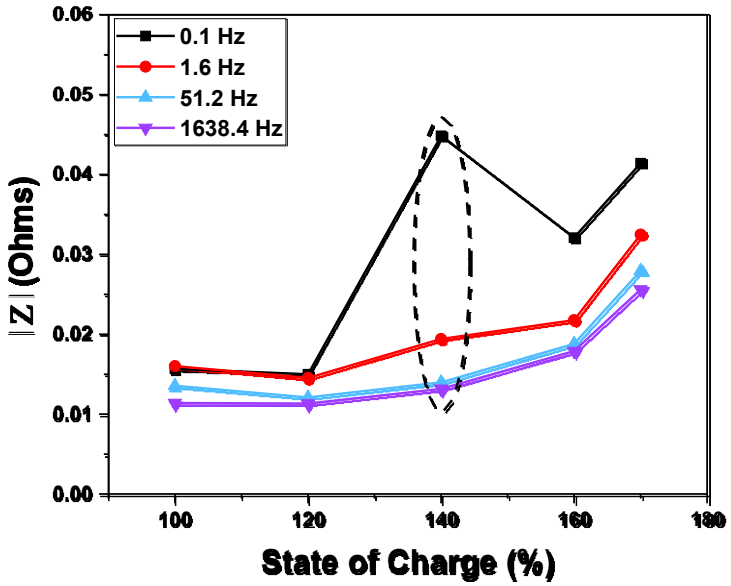

Figure 3: Scalar impedance results at varying frequencies during overcharge tests of NMC cells.

Figure 4 shows the results of equivalent circuit modeling of the complex impedance results in **Figure 2d**. R_{ohmic} represents general DC resistance within the cell, and remains constant until very high levels of overcharge, where a loss of electrical connectivity between the various cell components begins to overwhelm the cell and lead to a rise in general resistance. This is useful in identifying levels of overcharge where all operability of the cell begins to be lost. The charge transfer resistance (R_{CT}) is one of the more useful values in this analysis, as this represents the energy barrier for the transfer of lithium from solid state to ions in solution. The sudden change in R_{CT}, potentially represents bulk changes in the active material that lead to the loss in stability seen at higher levels of overcharge.

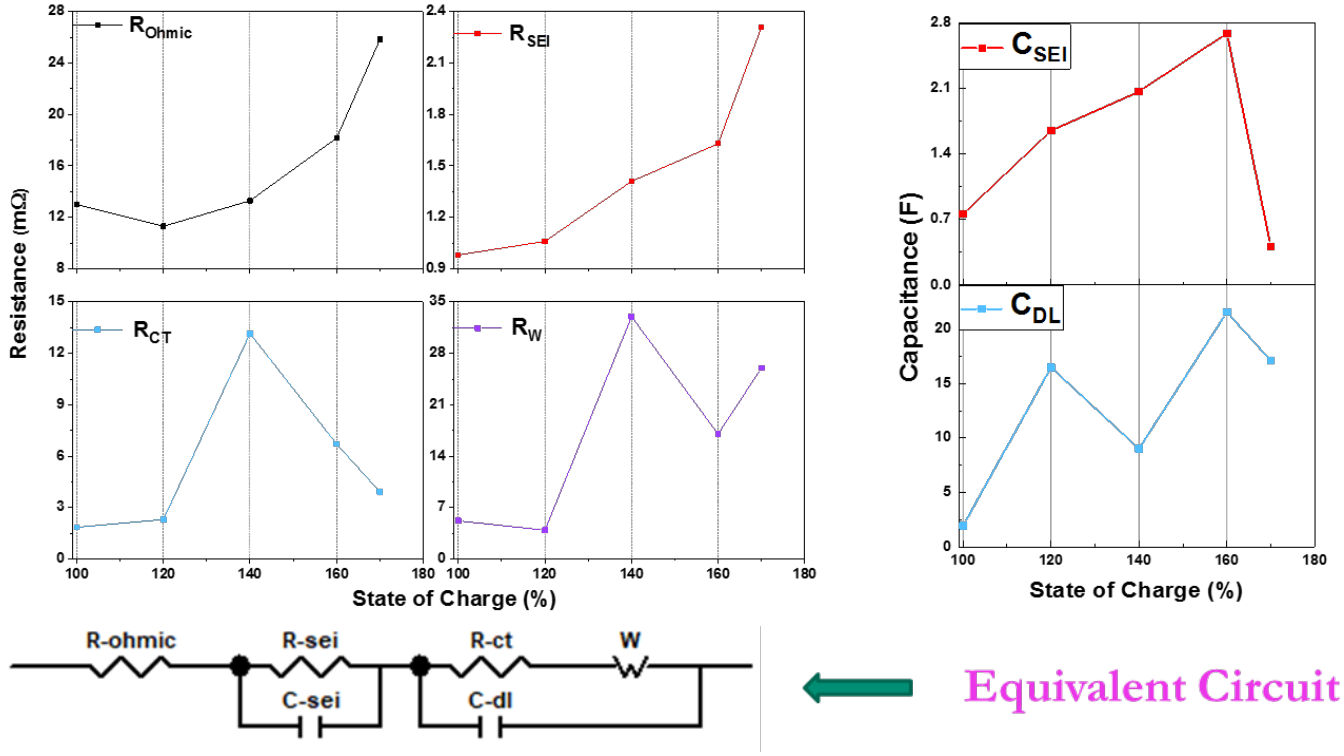

Figure 4: NMC In operando testing 170 percent SOC. Also shown is the common equivalent circuit used in evaluating batteries showing the SEI layer behaviors (R_{SEI} and C_{SEI}) charge transfer resistance (R_{ct}), double layer capacitance (C_{dl}) and Warburg impedance (W).

Partially overcharged cells that were still operable were cycled after overcharge testing to observe differential capacity changes that may be tracked to determine what amount of damage was done to a cell. These results are shown in **Figure 5**, showing the differential capacity collected during overcharge testing itself (left), and the post-test collection (right). Differential capacity collected during overcharge shows a distinct peak at ~134 percent SOC that correlates well to the transition that we observed in EIS data occurring between 120 and 140 percent SOC. This also tracks reasonably well with where temperature and voltage behavior changes in **Figure 1**.

Peak shifts in the cells cycled after partial overcharge exposure are observed in **Figure 5 (right)**. Similarly, this shows little change up to 120 percent total SOC, but at higher states of charge begins to show shifts in the peaks. This shows signs of loss of lithium inventory as well as active material from the cell, and is consistent with the bulk damage that was observed at these higher states of charge using impedance spectroscopy.

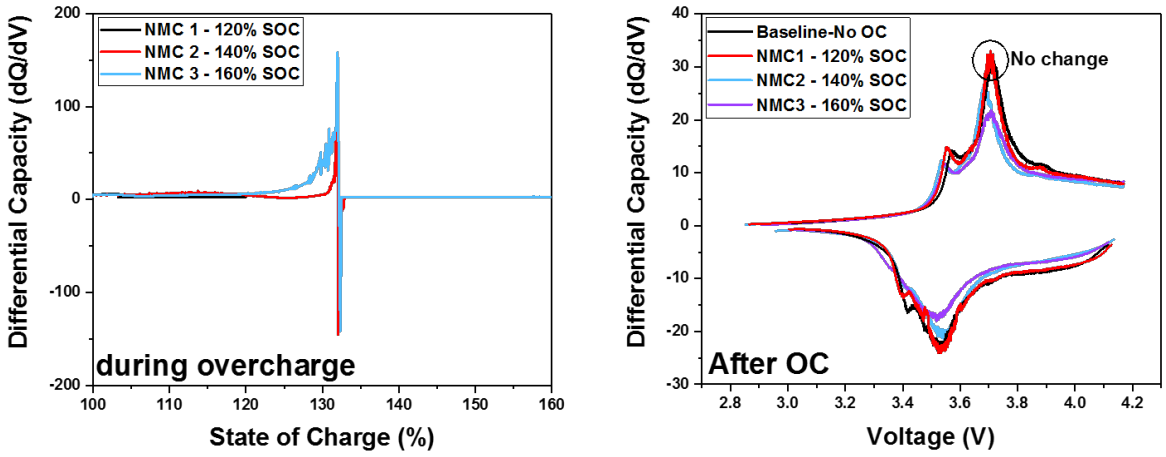

Figure 5: Differential capacity data on cells cycled during and after partial overcharge abuse tests.

Impedance monitoring was performed on more complex multi cell configurations as well. **Figure 6** shows these results in a 3S2P pack configuration, where the overcharge was applied to the central 2 cell parallel module. While the response in this case is not as strong, there is a distinct shift observed at lower frequencies. Response, however, was only observed at low frequencies. This establishes that low frequency, or even full spectrum impedance measurements will be necessary when using this technique on more complex pack formats.

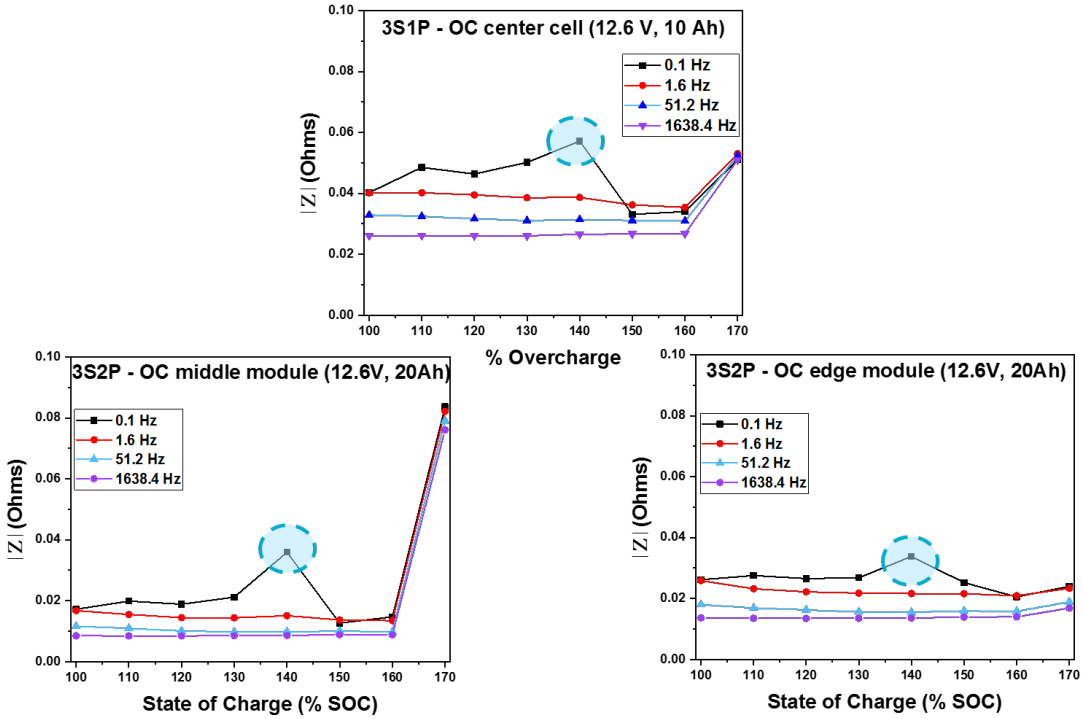

Figure 6: Comparison of multi cell configurations.

Figures 7-10 show the results of applying in-operando impedance measurements as well as differential capacity measurements to single cells exposed to elevated temperatures. The in-operando testing was accomplished by making measurements while the target cell was exposed to a 2 °C/min thermal ramp test until cell failure was reached, or a target temperature in the case of partial damage tests. **Figure 7** shows the voltage and temperature results at increasing temperatures. There is remarkably little voltage loss as the cell reaches high temperatures. Spotting this level of heat may be difficult if it occurs within a localized area of a battery pack.

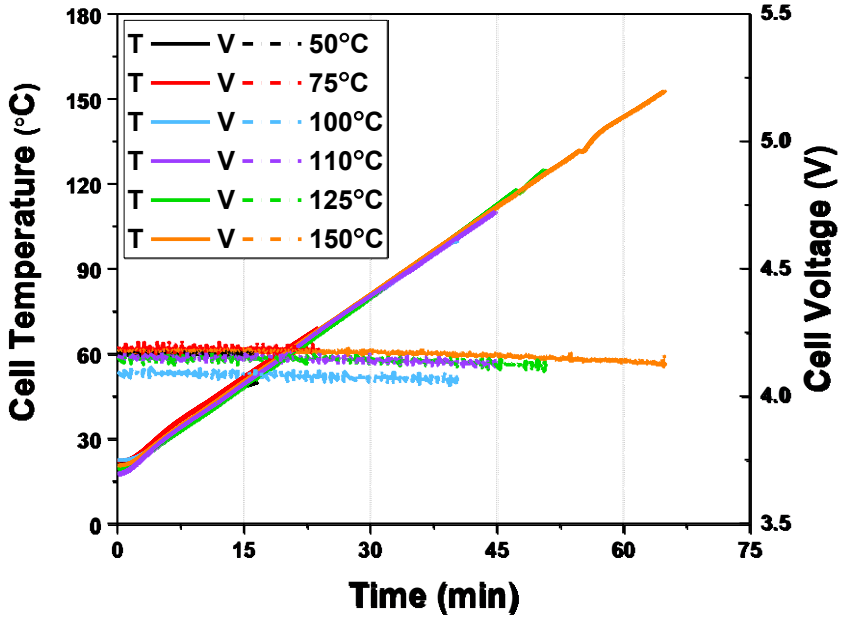

Figure 7: NMC comparison of thermal ramp and voltage behaviors.

Figure 8 and **Figure 9** show the in-operando EIS results while **Figure 10** shows the differential capacity results collected on cells after partial over temperature exposure. The complex impedance collected during the thermal ramp test (**Figure 8 left**) shows that relatively minor changes are observed up to 100 °C, however above that point significant changes begin to develop in the EIS curves. This points to the technique being most effective at detecting temperatures that approach dangerous levels, but would be unlikely to provide a signal at more moderate temperatures. **Figure 9** shows that nearly all frequencies show a significant change at temperatures above 100 °C, giving a strong detection signal as the cell approaches potentially dangerous temperatures.

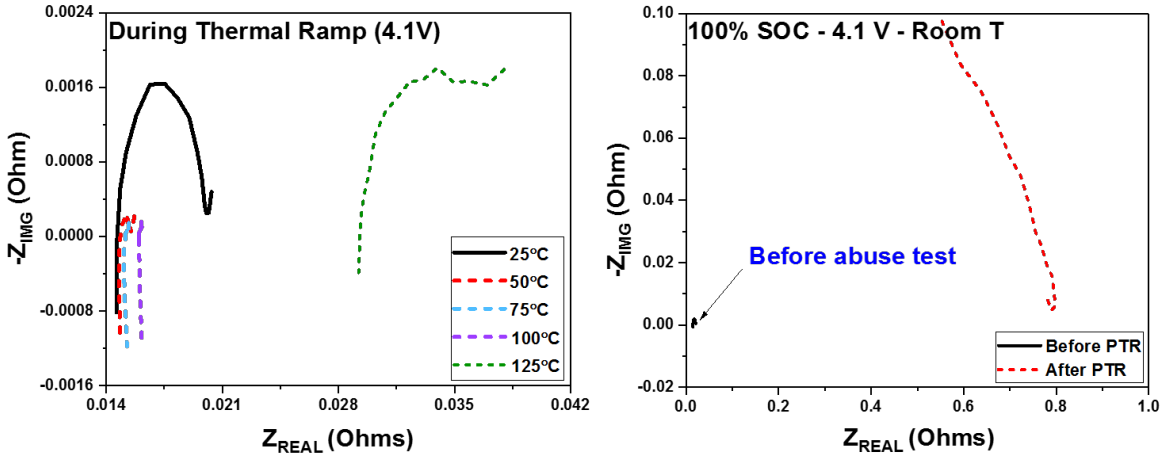

Figure 8: In-operando EIS measurements on partial thermal ramp test (PTR) up to 125 °C.

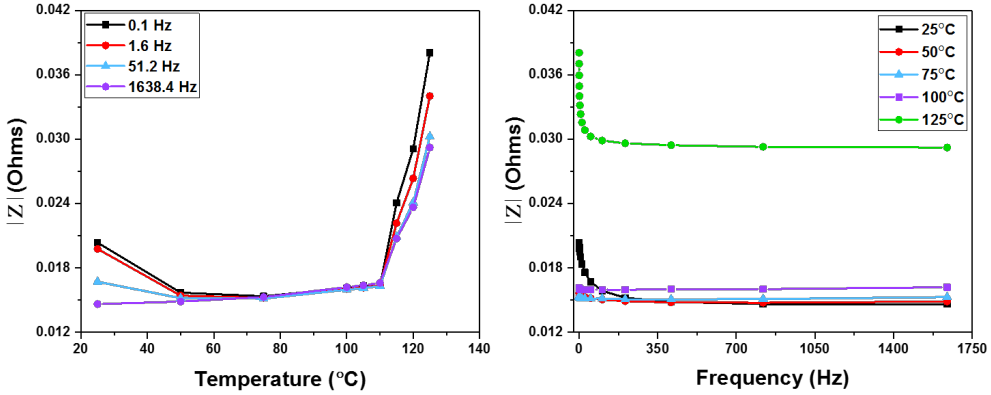

Figure 9: Bode plots of data in operando EIS measurements up to 125 °C.

Figure 10 shows differential capacity plots collected after partial thermal ramp testing in the case of cell that are still operable. Similar to the complex impedance plots, this shows little change until reaching temperatures above 100 °C, where we begin to see signs of significant damage to the battery. The overall single cell results with NMC suggest that potential damage is easily observable once temperatures are increased to these severe levels. However, more moderate increases would likely be difficult to detect. The complex impedance does show some potentially trackable behaviors; however, they are at a level that may be difficult to identify with an embedded tool.

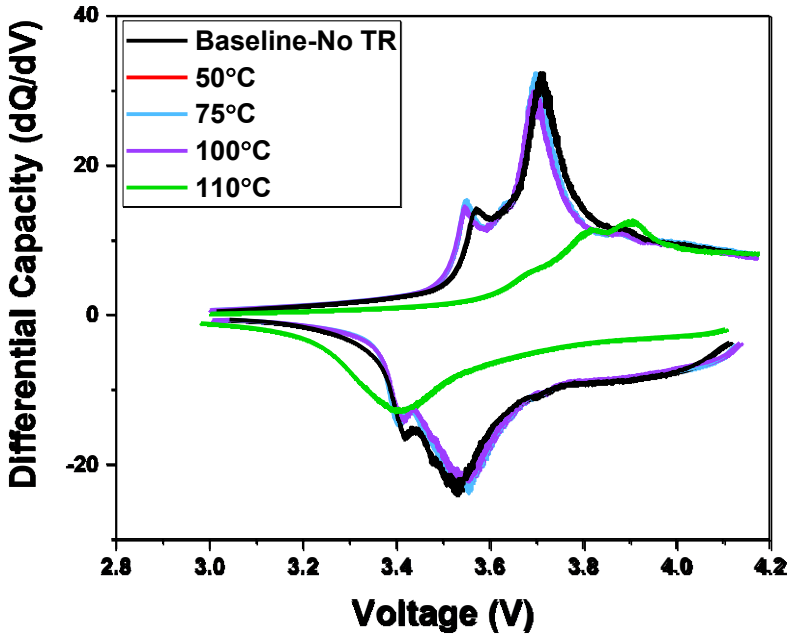

Figure 10: Differential capacity measurements of NMC pouch cells made after exposure to elevated temperatures.

Work was also performed to evaluate the detection of the elevated temperature of a single cell within complex multi cell packs. The results of this work are shown in **Figures 11-14**. This work looks at packs of varying complexity, including increasing amounts of cells in parallel running from 1S3P to 1S6P packs. Series strings of up to 5 cells were tested, as well as modular 3S2P packs. In all cases a single cell was exposed to the thermal ramp test while the whole pack impedance was monitored.

Parallel pack results in **Figure 11** show the impact of increasing the number of modules in parallel on the detection capabilities of the impedance measurement. In all cases, we were able to observe similar effects at elevated temperature. Increases in the scalar impedance similar to those seen for single cells were observed at temperatures above 110 °C. However, the parallel packs did further limit the detection capabilities at lower temperatures. The low temperature results, particularly in the window from 40 to 100 °C, were nearly flat. The changes brought on by elevated temperature in this case are so catastrophic that they resist being washed out by the large number of cells in parallel, however the more subtle changes that occur at lower temperatures become functionally difficult to detect. There were also shifts in the temperature at which the major changes to the EIS data was observed, potentially changing the level of detectability in large packs.

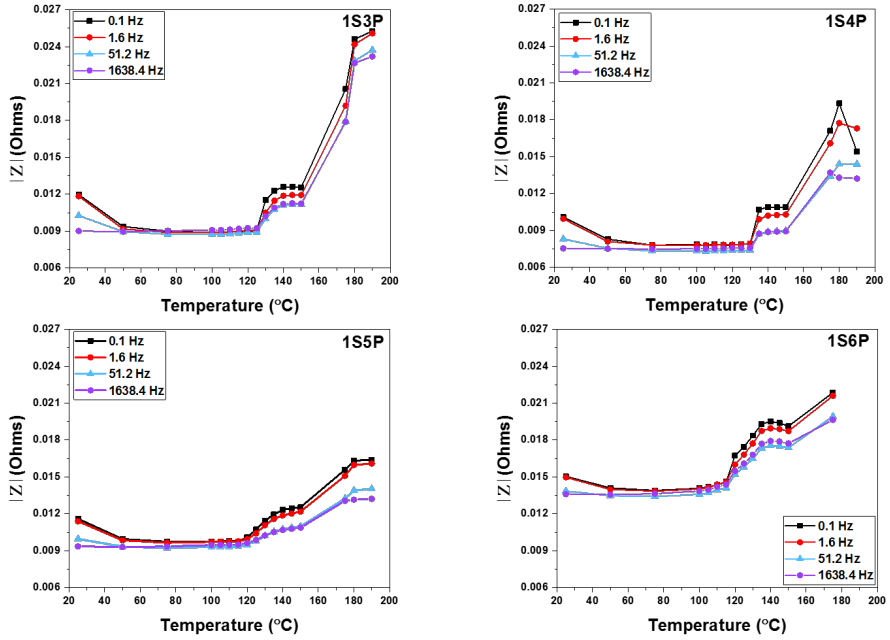

Figure 11: Comparison of in operando measurements made on parallel packs.

Similar to parallel strings, series string results shown in **Figure 12** have good levels of detection at high temperatures. In this case, a transition is readily observed at 120 °C and above, as the target cell approaches thermal runaway. There is some measurable signal at lower temperatures, however similar to the single cell tests, this is much more subtle than the high temperature behavior.

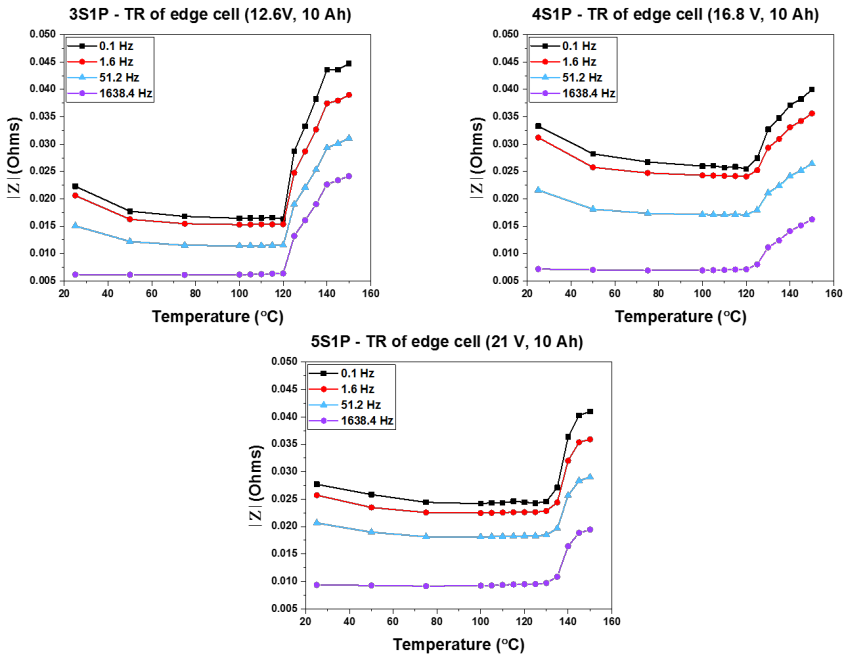

Figure 12: Comparison of in operando measurements made on series packs.

Figure 13 shows the results of the complex multi module pack. In this case, the battery was a series of three modules each made up of two cells in parallel. The testing for **Figure 13(a)** was performed by applying the thermal ramp to a single cell within the center module, while in **Figure 13(b)** it was applied to an entire two cell module. At this level of complexity, we begin to see the signal becoming washed out as the resistances detected within the entire pack begin to counteract any behaviors observed due to cell failure. This points to a strategy where a detection method would likely have to raster between individual modules for meaningful detection, a demonstration of which is a potential avenue for further development.

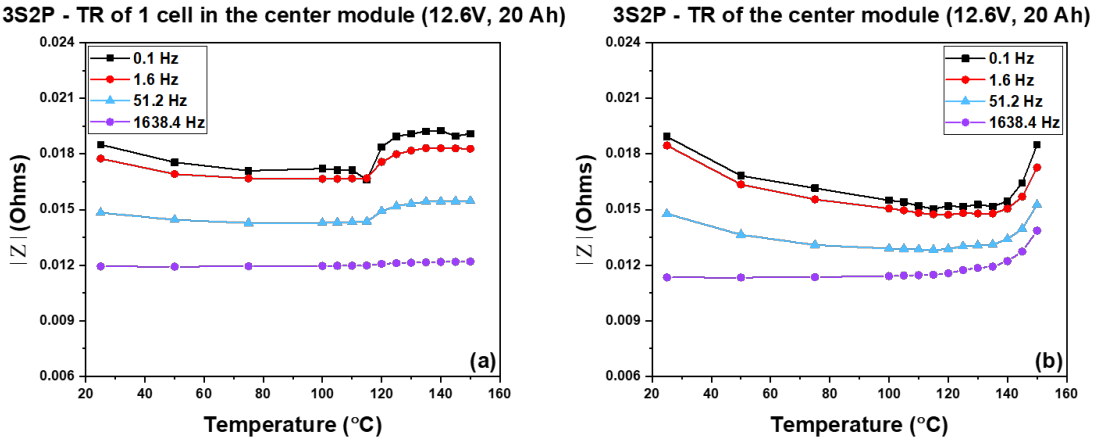

Figure 13: In operando measurements of 3S2P packs.

Lithium iron phosphate (LFP) cathode chemistries are generally accepted to be a safer alternative to conventional lithium ion chemistries due to the more subdued thermal runaway response, owed to the stable nature of the cathode. However, LFP batteries do have some unique interactions with overcharge, as previous abuse testing work has demonstrated that the cells are prone to quickly reach elevated voltages when exposed to overcharge and lead to subsequent failure of the cell. This presents a case to case study to determine the applicability of this technique when applied to chemistries beyond standard mixed metal oxide cathode materials.

Figures 14-17 show the results collected on the overcharge of LFP single cells. **Figure 14** illustrates the voltage and temperature response of the cells with overcharge conditions. In order to establish the behaviors at different levels of overcharge, cells were charged to levels of 105-120 percent SOC. The LFP cells used for this study typically failed above 120 percent SOC and showed behaviors that changed rapidly with even low levels of overcharge. Note that cells with nominal voltage of 3.2 V rapidly rise in voltage, reaching over 8 V with only 120 percent total state of charge. This indicates that relatively small amounts of overcharge may be able to damage the cells, which may be problematic in a larger system as some small amount of overcharging may occur over the life of a battery due to imbalance between various cells within the battery pack.

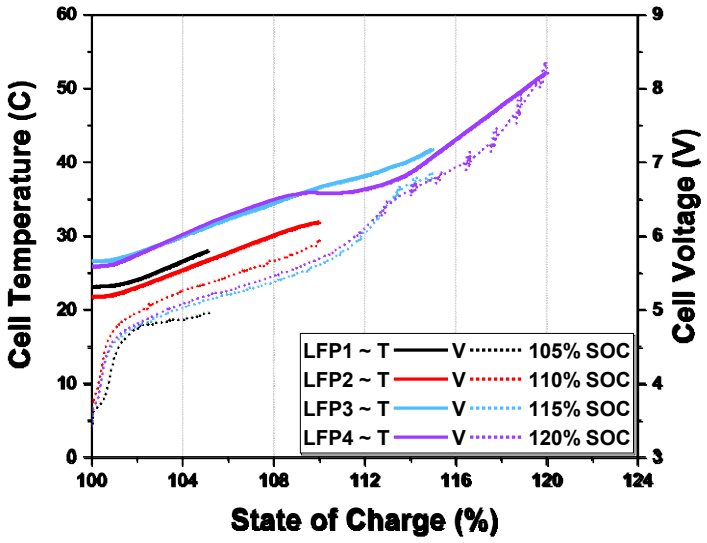

Figure 14: Overcharge testing of LFP cells. Different cells were charged to increasing levels of overcharge to determine variance in behaviors with overcharge level.

Figure 15 shows the complex impedance results during in-operando testing of a single LFP cell. This shows smaller initial changes up to 110 percent SOC, but more significant changes above that point are identified. We see significant shifts in the behavior at 115 percent and 120 percent SOC. This also corresponds to a significant increase in the voltages, noted on the figure inset. The values obtained from equivalent circuit modeling are shown in **Figure 16**. The ohmic resistance rises with even small increases of state of charge, suggesting that even moderate overcharging is doing significant damage to the cell. The charge transfer resistance shows a starker transition, which occurs at 115 percent SOC. This also corresponds to an inflection in the cell voltage observed in **Figure 14**, suggesting a physical transition at this point.

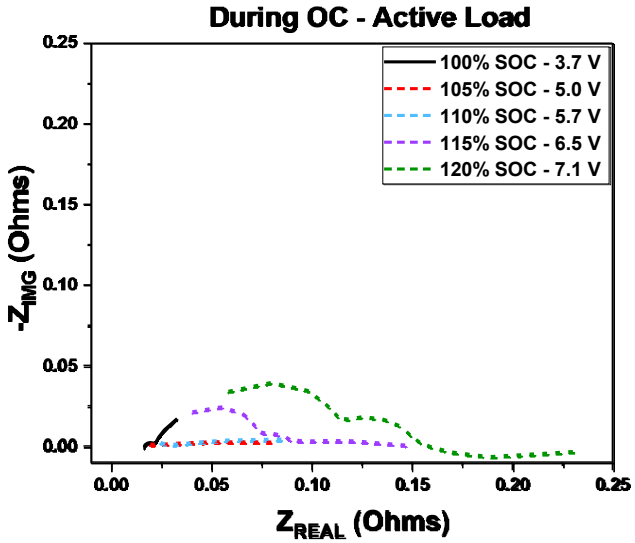

Figure 15: In operando EIS taken during overcharge of LFP cells.

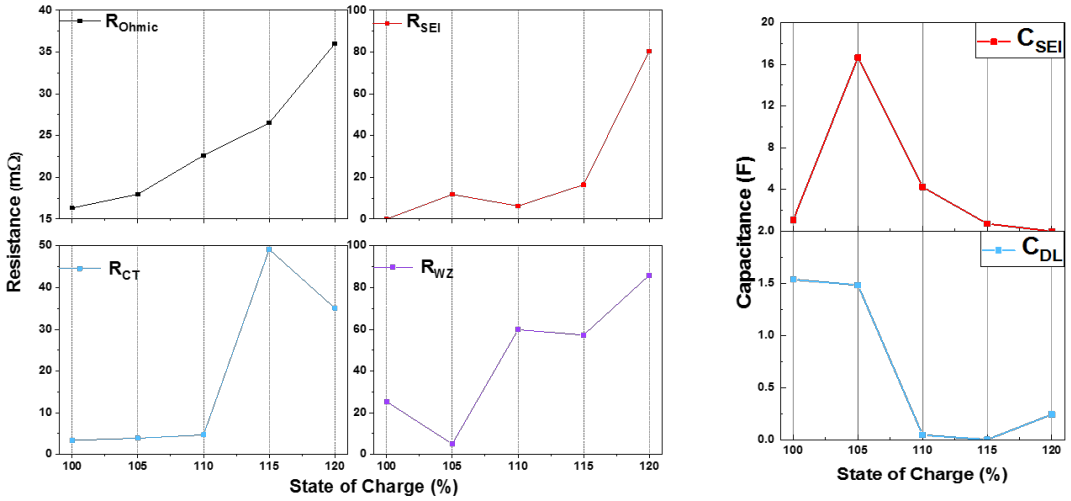

Figure 16: Equivalent circuit parameters from overcharged LFP cells determined using the equivalent circuit model shown in Figure 4.

Figure 17 shows the results of differential capacity measurements taken during the overcharge test (left) and on cells after overcharge testing was performed (right). The analysis of the overcharge data suggests that damage to the cell begins almost immediately with application of overcharge, with a peak occurring at ~104 percent SOC, and another occurring at ~113 percent SOC. The measurements taken post-test support this as well, showing significant changes to the peaks after testing at 105 percent SOC and continual shifts after that. The impetus for failure detection in LFP cells is lower, owing to its more subdued failure response, however this presents performance implications for LFP cells in a large system. It is difficult to fully maintain perfect cell balance over the lifetime of a large battery pack, and some limited overcharging may occur. While typically this is low, the data here suggests that even those low amounts of overcharge may have a physical impact on the cell that could be compounded over time.

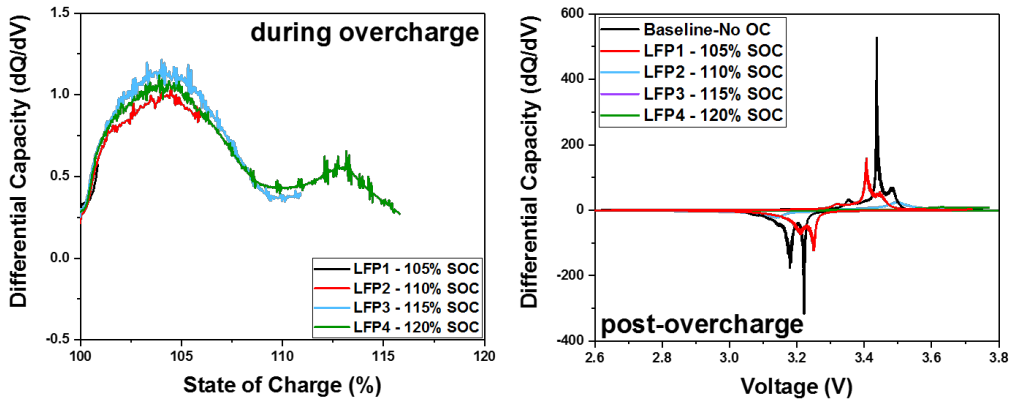

Figure 17: Differential capacity measurements during (left) as well as before and after (right) single cell overcharge.

Battery state of stability evaluation under mild abuse and aging scenarios at INL

High impedance short circuits within cells, capacity imbalance in a module and cell-to-cell heterogeneity within a string, present several means of failures that can limit performance, and potentially develop into a more serious condition over time. Impedance analysis presents a potential tool that may be able to detect these subtle changes and identify problematic cells or module before they develop into a safety hazard or performance issues. INL has evaluated IMB's diagnostic performance for the following three cases considering immediate, mid and long-term performance and safety concerns. The main objective was to evaluate IMB's operational bounds of detectability under these different abnormal or faulty conditions.

A. Short detection in a single cell setting with aging- focus on immediate safety concerns
B. Capacity imbalance detection in string settings (10S, 6S, and 4S)- focus on mid- and long-term safety concerns
C. Detection of aged cell (up to 20%) in string settings (10S1P and 1S4P) focus on mid- and long-term safety concerns

The lessons from these case studies provide a better understanding on battery safety following a crash or following aggressive charging (especially for aged packs). The knowledge could also furnish distinct benefit for first responder support. All testing at INL was performed on automotive grade 16 Ah NMC-graphite pouch cells.

A. Short detection in single cell setting with aging

Figure 18 shows the general performance of the impedance measurement tool, and **Figure 19** shows general information of how the tool can be used to detect a potential short circuit event. The Warburg component is used in this case to track the changes in conductivity that occurs when a short circuit event is applied to the cell. The short circuit scenarios were created by applying external loads at a desired rate e.g., C/100, C/10 or C/5. The safety hazard due to shorts like these could manifest immediately or remain potent for days or even weeks depending on the severity of the short. But, immediate detection of such shorts is highly desirable to avoid expensive consequences. **Figure 19** (right) shows this most dramatically with a C/5 external short circuit applied to the cell and the resultant impedance changes tracked. These results show a significant variation at low frequencies, with a C/5 short and100 percent SOC, but as the state of charge changes and current of the external short drops, the change in impedance signal appears to go down. Variations in the Warburg tail were more detectable at shorts equal to or larger than the C/10 charge rate. Reliable detection and quantification of these changes through IMB beyond its inherent measurement uncertainty is a crucial requirement and needs to be evaluated.

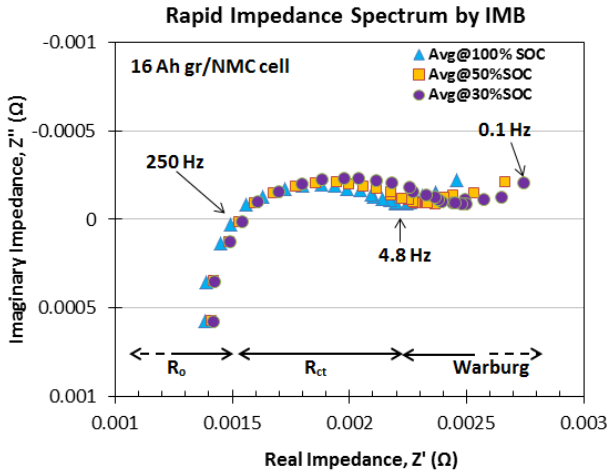

Figure 18: Results showing the performance of the IMB.

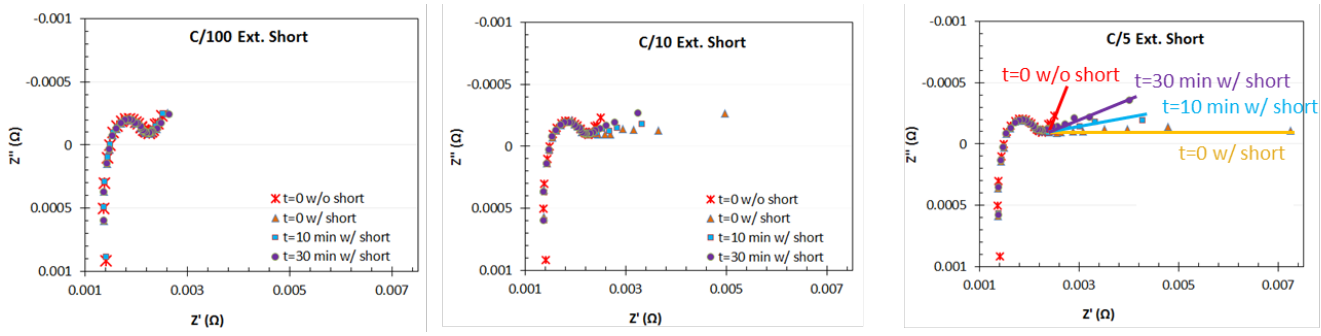

Figure 19: Results showing the changes to the Warburg impedance components with added short circuits.

The uncertainty associated with IMB that occurs between measurements can be characterized by limit of detection (LOD) and limit of quantitation (LOQ). The LOD equates to values that are at least three times the standard deviation away from the average of a set of measurements. LOQ is typically defined as 10 times the standard deviation of baseline measurements. The complex magnitude of impedance, $|Z| = \sqrt{Z'^2 + Z''^2}$, was used as representative measurements within the frequency of interest for each case. **Figure 20** shows the performance of IMB in terms of LOD and LOQ as the state of charge changes. The standard deviation of 10 back-to-back IMB measurements at each SOC set point was used for LOD and LOQ. **Figure 20** shows that IMB measurement is noisier at lower SOC (i.e., higher LOD and LOQ values) and thus, would provide lower level detectability. Higher SOC, e.g., 100 percent retains better detectability than the lower SOCs. Aged cells may impact this as well as they effectively reduce the total stored energy and increase impedance of the cell. **Figures 21-32** present an in-depth study of how the detectability of various shorts changes with cell aging and applied short circuit current. Here, ΔZ is the difference between the baseline (without short at rest) and the signal of interest (with applied short).

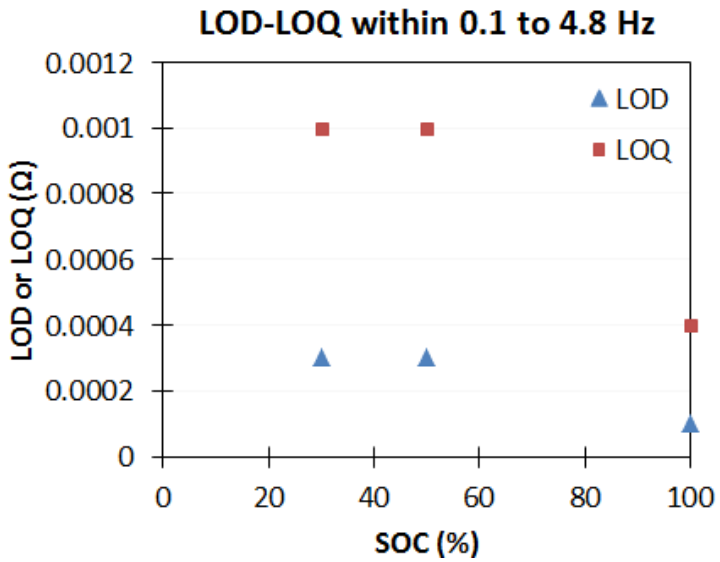

Figure 20: Performance of the IMB detecting shorts at varying SOC.

Figures 21-24 show the shorts applied at 100 percent SOC with various levels of cell aging. Cells were calendar aged at 4.2V at different temperatures (up to 55°C) to obtain the desired extent of capacity fade, e.g., 5 percent, 10 percent, and 20 percent. Fresh cells, shown in **Figure 21** shows that the low frequencies have points above both the LOD and LOQ for C/5 and C/10 shorts. The detectability on C/100 shorts is less clear, with some points rising above the LOD at low frequencies. However, the difference in measurements could not exceed the LOQ line, indicating very weak quantifiably at C/100. Increasing the level of cell aging to 5 percent does not noticeably affect this trend, with strong detectability for C/10 and C/5 shorts and murkier results at C/100.

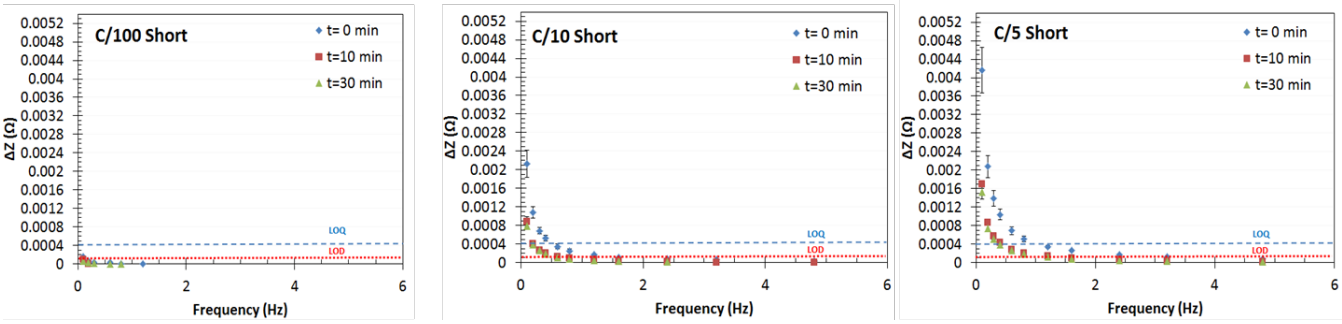

Figure 21: Short circuit data collected on a cell at 100 percent SOC with 0 percent cell aging.

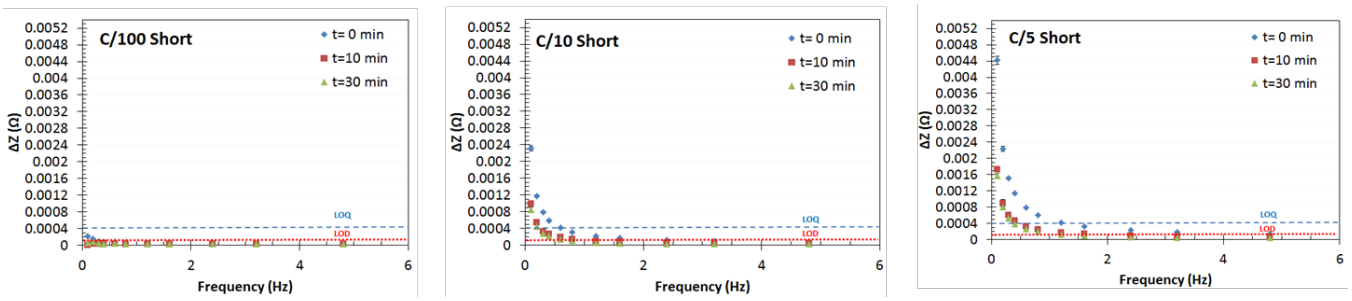

Figure 22: Applied shorts at 100 percentSOC and 5 percent aging.

Increasing the aging to 10 percent shows similar trends (**Figure 23**), however we do begin to see some more variability in the measurements as well. Further, at C/100 we see the signal fall below levels that would be readily detectable. 20 percent aging (**Figure 24**) also follow this trend, however we begin to see a large amount of variability in the results, with large error bars (1σ variation from triplicate of cells) particularly when the short is initially applied. Irrespective of the cell age, a stronger ΔZ was always obtained immediately after the short, which weakens slightly afterwards with time.

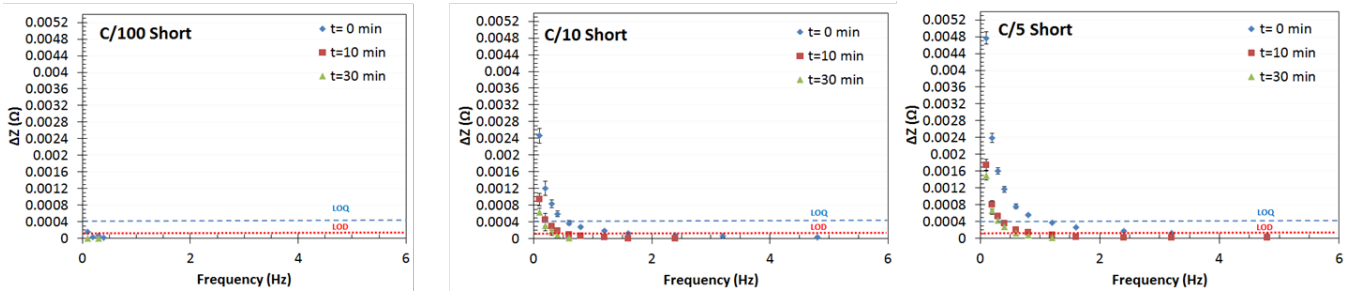

Figure 23: Applied shorts at 100 percent SOC and 10 percent aging.

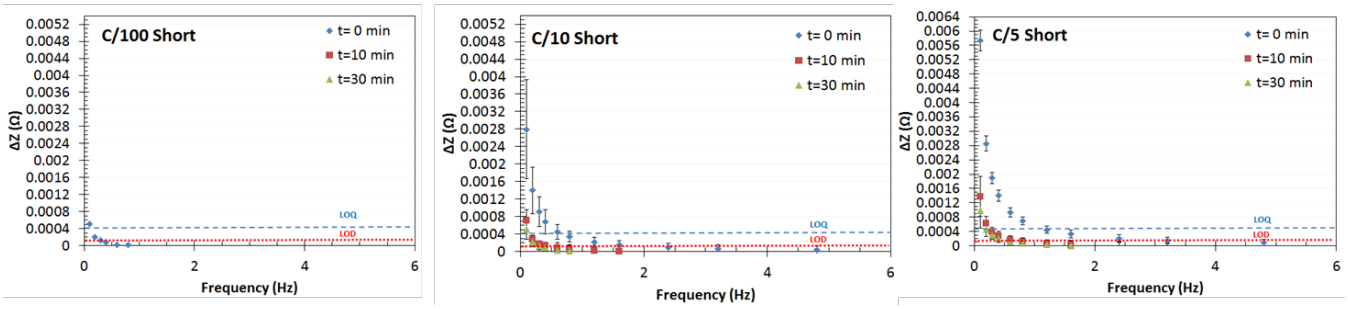

Figure 24: Applied shorts at 100 percent SOC and 20 percent aging.

Testing was performed at 50 percent SOC as well and in general the short detection became more difficult at the lower state of charge. These results are presented in **Figures 25 to 28**. With fresh cells (**Figure 25**), the detectability is still strong with C/5 short circuits, and the lowest frequencies still show good detection at C/10. However, the C/100 short circuits do not rise above the detection thresholds.

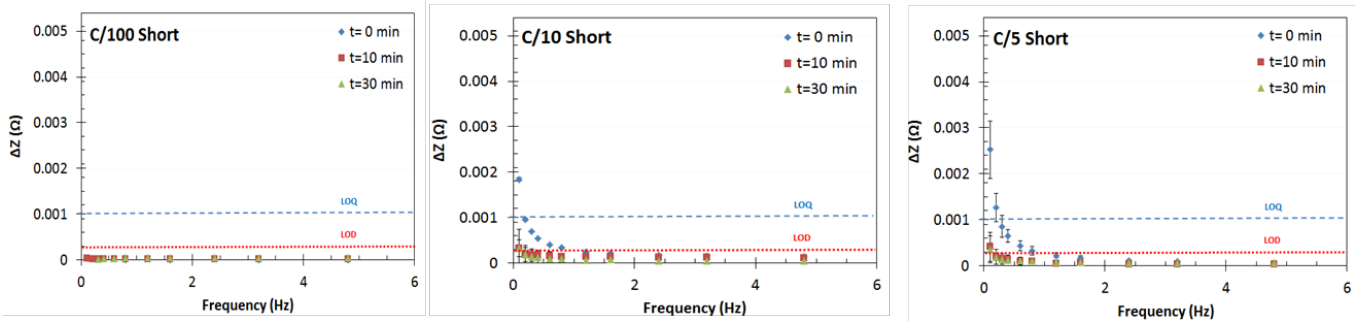

Figure 25: Applied shorts at 50 percent SOC and 0 percent aging.

The same trend continues at 5 percent aging, with the 5 percent aging results showing little difference from the fresh cells. The developing trend is that small amounts of aging, as expected, do not change the cells significantly enough to see a marked change in the cell behavior. We also see continued behavior that the short is most easily detected at the moment the short occurs, however the 10-minute and 30-minute behaviors do remain above the lowest detection thresholds.

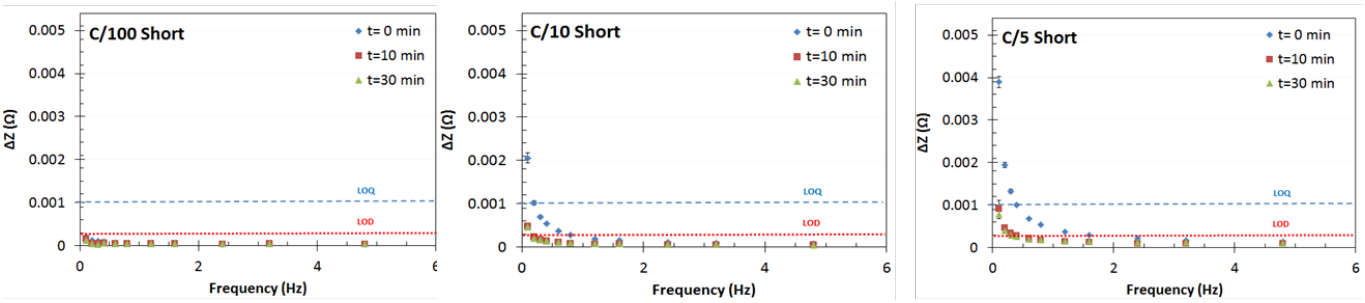

Figure 26: Applied shorts at 50 percent SOC and 5 percent aging.

Higher levels of aging are seen in **Figures 27 and 28**. The general patterns are similar like those seen in the cells with lower amounts of aging, however we do begin to see more variability in the measurements, particularly in the measurements immediately after application of the applied short circuit.

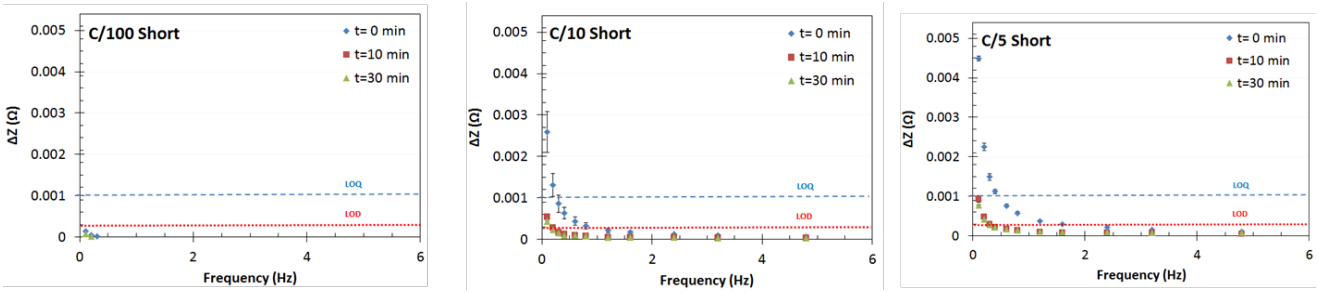

Figure 27: Applied shorts at 50 percent SOC and 10 percent aging.

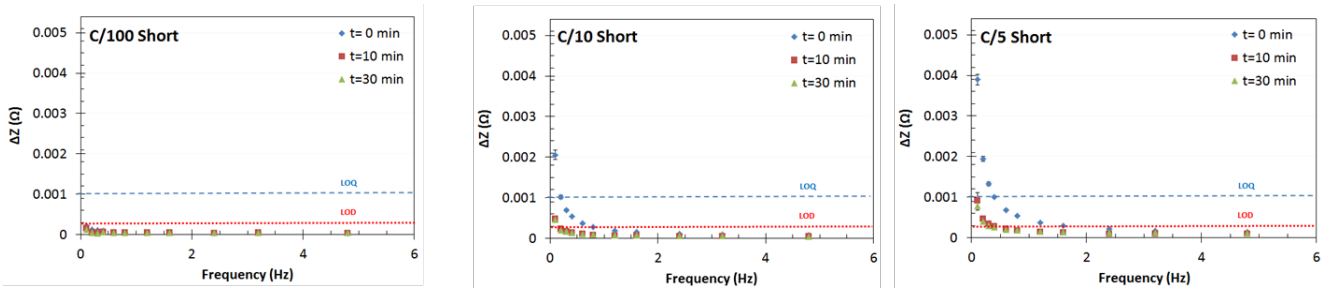

Figure 28: Applied shorts at 50 percent SOC and 20 percent aging.

The lowest SOC measured in this study was 30 percent SOC and this work is shown in **Figures 29-32**. These lowest states of charge are expected to provide the greatest challenge to measurement fidelity. The lower SOCs studied on fresh cells and cells with 5 percent aging are seen in **Figures 29 and 30**. These results show the lowest frequencies are still able to detect the short immediately after it occurs for C/10 and C/5 shorts. However, the detectability begins to drop below detectable thresholds 10 minutes after the short occurs, particularly for the C/10 short. After 10 minutes, the C/10 short has fallen below the detection threshold in both cases. The C/5 short remains above the lowest detection threshold after 10 minutes, but has fallen below the LOQ. The C/100 short is below the detection threshold even immediately after the short occurs.

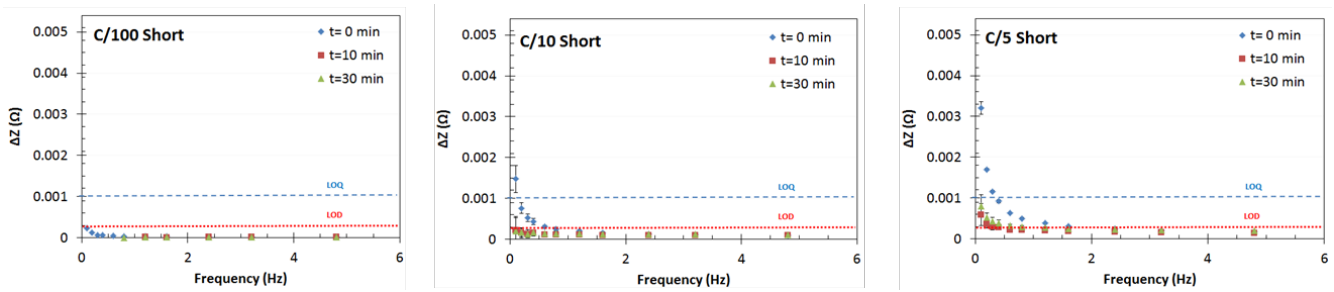

Figure 29: Applied shorts at 30 percent SOC and 0 percent aging.

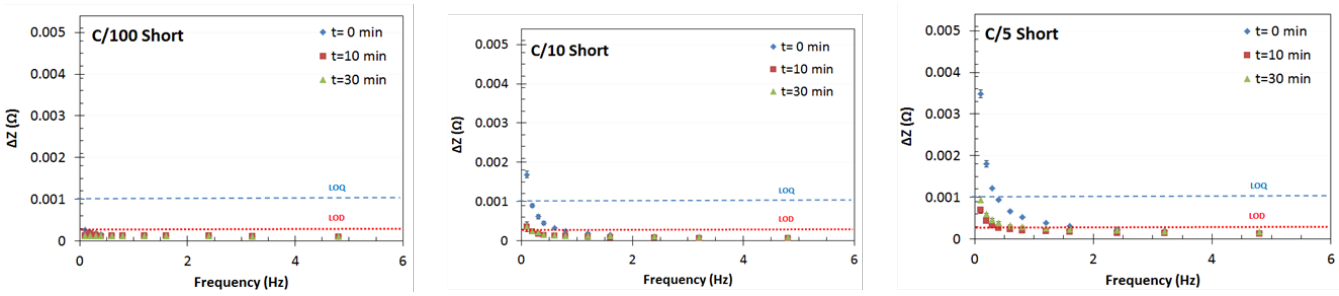

Figure 30: Applied shorts at 30 percent SOC and 5 percent aging.

At the higher levels of aging (**Figures 31 and 32**) some effects of aging are seen in the C/10 and C/5 shorts which provides the benefit of bringing all conditions above the lowest detection levels in all cases for these shorts. Similarly, to other aged cells, we begin to see more noise in measurements, with greater error bars in particular on the measurements made right after the short.

These cells exhibit the difficulty of detecting the C/100 short that is observed in other cells as well. In all cases, the C/100 short does not rise above the lowest detection thresholds. There are some trends that can be observed, particularly on fresh and 5 percent aged cells where the change in resistance rises at lower frequencies, but it is generally below the LOD in these cases.

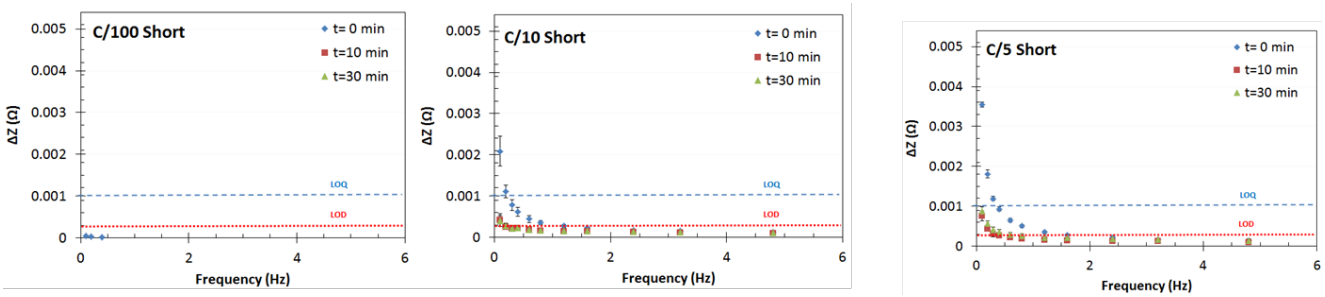

Figure 31: Applied shorts at 30 percent SOC and 10 percent aging.

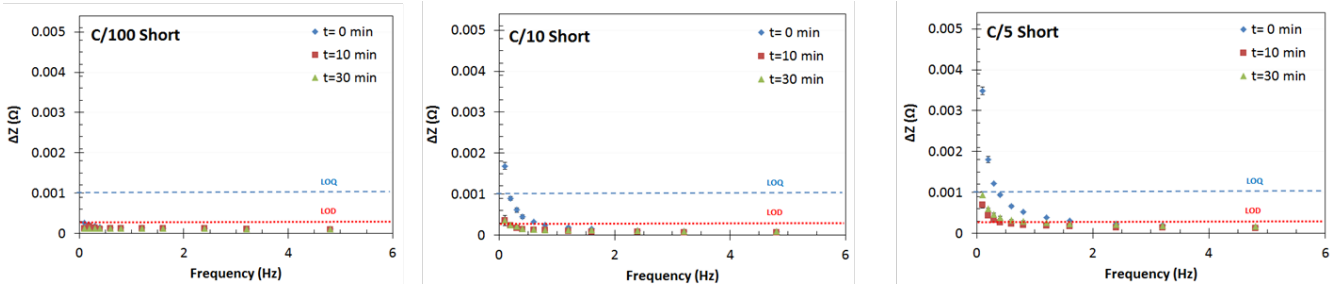

Figure 32: Applied shorts at 30 percent SOC and 20 percent aging.

B. Capacity imbalance detection in string settings (10S, 6S, and 4S)

Damaged or abnormal cell(s) within a string or pack could self-discharge due to internal or external shorting and potentially create a capacity imbalanced string or pack. The most distinct alignment relates to long-term safety especially for aggressively used vehicle and following some crash conditions. If undetected, this could potentially limit the pack performance and in the worst-case scenario could create severe safety hazards. Thus, detection of an unbalanced string or pack as soon as it happens is crucial. In this case study, INL built such unbalanced strings and examined IMB's detection capability. Serially connected strings with three different lengths, e.g., 10S, 6S and 4S, were evaluated at different SOCs, e.g., 100 percent, 50 percent and 30 percent. A single unbalanced cell with 10 percent and 20 percent capacity difference than the other cells were placed within the strings. **Figure 33** shows the experimental set up with 4S string setting. An individual string was fully charged and then discharged to the desired SOC at a C/3 rate. Then a single cell was discharged at a C/20 rate to obtain the desired capacity imbalance, e.g., 10 percent and 20 percent less than the rest of the cells in the string.

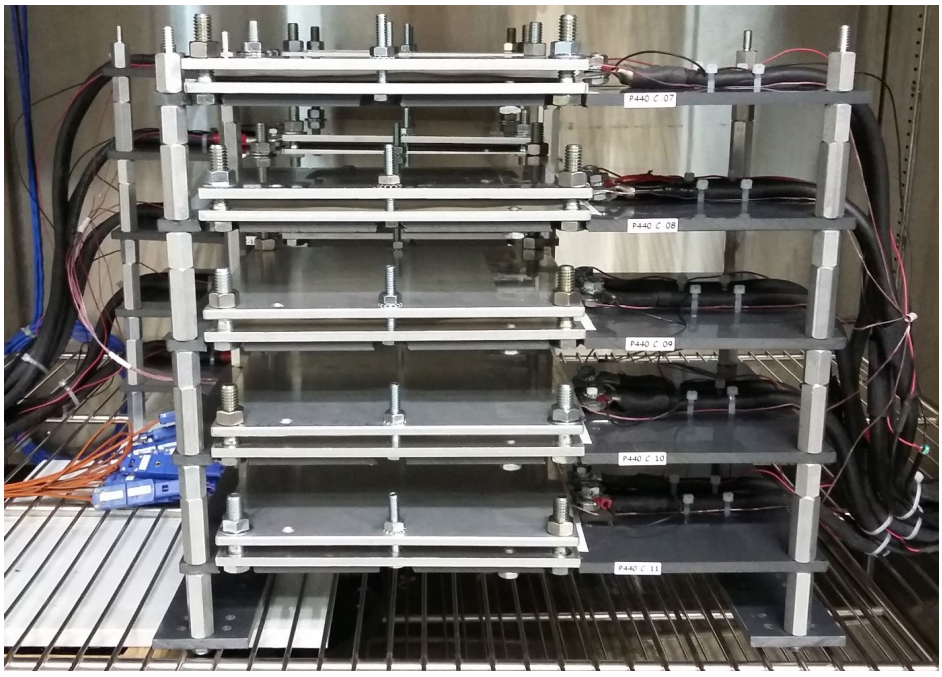

Figure 33: A 4S1P string for capacity imbalanace detection test.

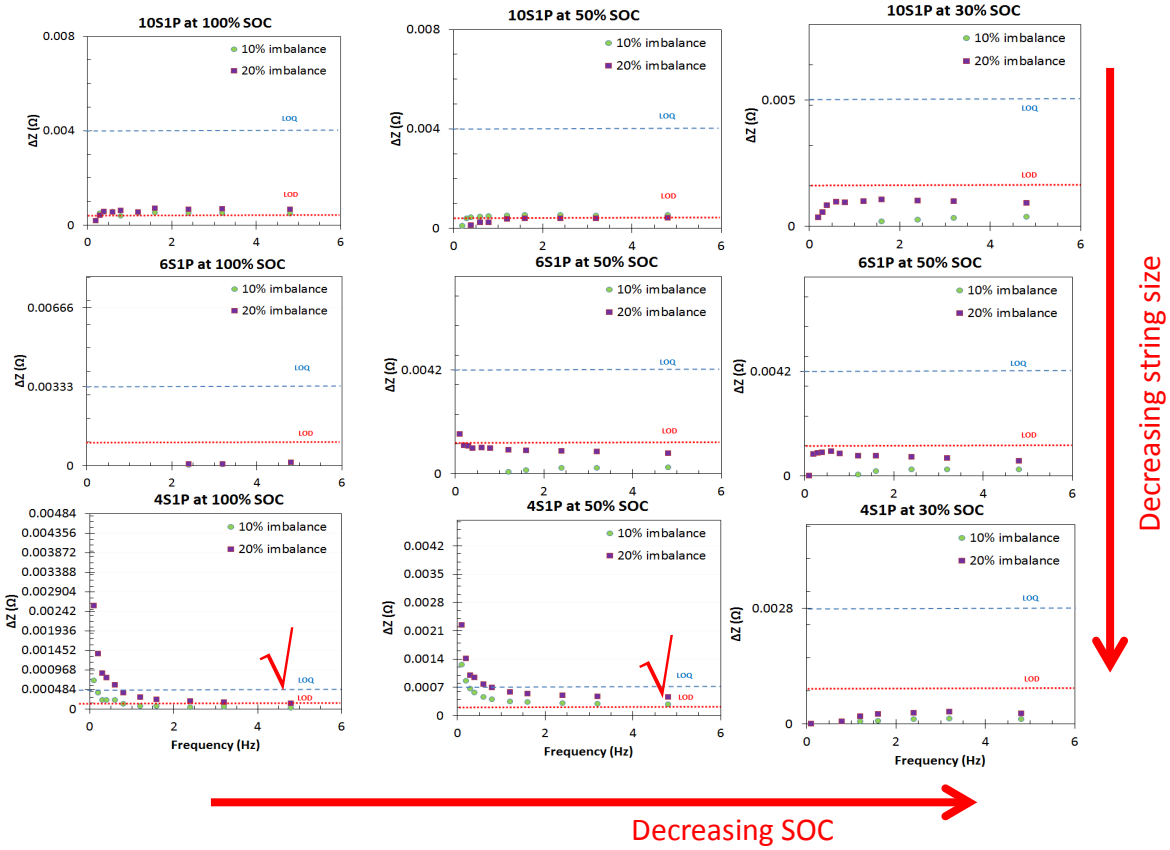

Figure 34: Summary of the detection capability of IMB for capacity imbalance strings.

Figure 34 summarizes IMB's performance in detecting a single unbalanced cell in serially connected strings (up to 10S) at different SOCs. Like before, the analysis was performed in terms of LOD and LOQ based on the complex magnitude of impedance, Z. The LOD and LOQ values are overlaid in Fig. 34, which were obtained from multiple repeated measurements in different string settings at different SOCs. In general, we observed lower detectability at lower SOCs as compared to higher SOCs. **Figure 34** shows the ΔZ values at different frequencies for the different string settings and with different level of capacity imbalance. The ΔZ is the difference in Z between the baselines (without imbalance at rest condition) and the signal of interest (w/ different extent of imbalance). In general, IMB's detection capability suffers at lower SOCs. For instance, the ΔZ rise above the LOD line for the 10S string at 100 percent SOC indicating its detectability. However, the differentiating signal remains below the LOQ line which suggests that the signal cannot be readily quantifiable. The situation becomes worse with lower SOC. For example, the 10S string imbalance cannot be detectable and quantifiable at 30 percent SOC (i.e., ΔZ at all frequencies remains below the LOD and LOQ line).

Increasing the string size also makes imbalance detection more difficult. **Figure 34** shows that cell imbalance can be detectable and readily quantifiable only for the smallest string (4S) and at higher SOC window (50%-100%) in the lower frequency range. Moreover, the ΔZ signal remained consistently stronger for the higher imbalance (20% single cell imbalance) compared to the lower one (10% single cell imbalance). Such a detection limitation on string size implies that a modular detection algorithm with IMB could be implemented in larger string settings for overall pack imbalance evaluation.

C. Detection of aged cell (up to 20%) in string settings (10S1P and 1S4P)

Cell-to-cell variability, caused by heterogeneous aging, is a key concern for aged battery packs as it may precede potential fault associated shorts from fast charging, or localized elevated temperature. In this case study, we introduced different cell-to-cell variability in series (10S1P) and parallel (1S4P) strings and evaluated IMB's detection capability. For both the series and parallel string settings, we introduced up to 3 aged cells with 20 percent and 5 percent capacity fade. For example, the 10S1P string had 7 unaged cell and 3, 20 percent aged cell in series. Similarly, the 4S1P string contained 1 fresh cell and 3, 20 percent aged cell in parallel.

Figure 35 shows the changes in impedance with different extent of aging in the 10S1P strings. The real part of impedance (Z′) in the higher frequency domain is more sensitive to the increased cell-to-cell variability. Thus, the real part of impedance (Z′) was considered as the basis for evaluating the detection limits of IMB in the high frequency domain (50 Hz to 1638Hz). **Figures 36-39** overlaid the LOD and LOQ values with ΔZ′. The Δ Z′ is the difference in Z′ between the baselines (10S1P or 1S4P without any heterogeneity, i.e., all fresh or unaged cells) and the signal of interest (10S1P or 1S4P with different levels of heterogeneity). The uncertainty of IMB measurements (lower LOD and LOQ values) remained very low for the series strings, irrespective of SOC as shown in **Figures 36-37**. The higher impedance associated with 10S1P could primarily be attributed to this better performance of IMB.

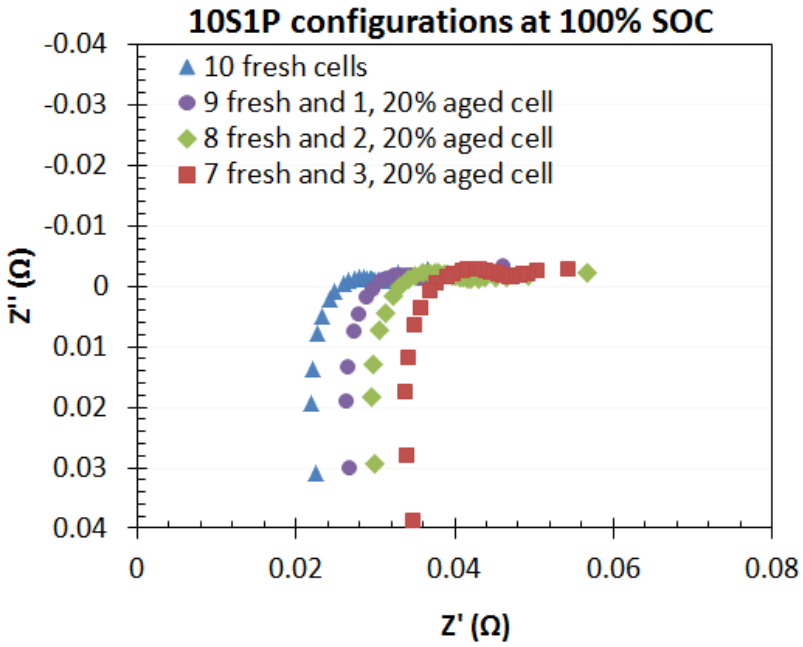

Figure 35: Results showing the performance of the IMB in string settings.

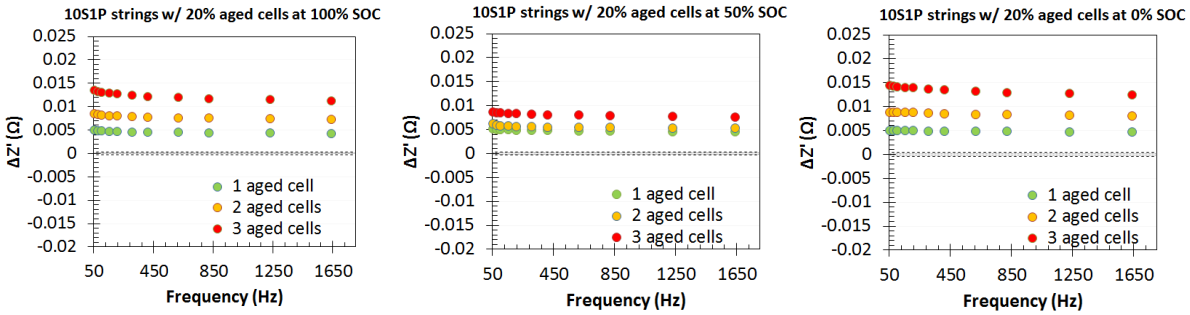

Figure 36: Results showing the detection capability of IMB with 20 percent cell-to-cell variability in 10S1P string configurations.

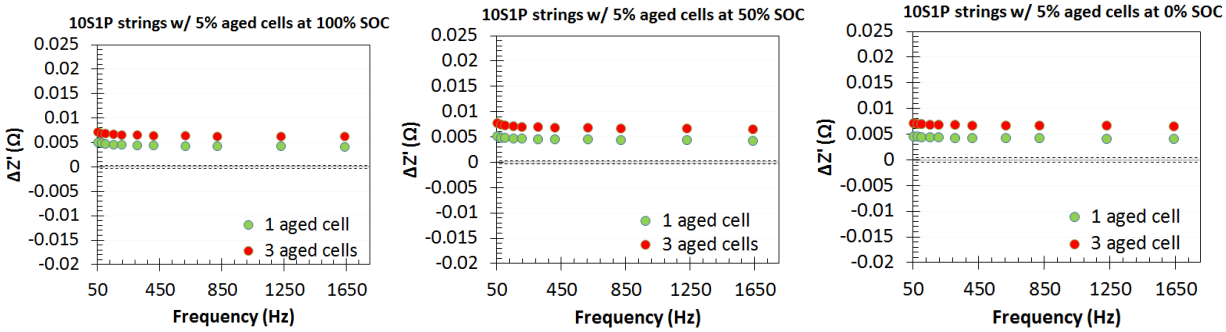

Figure 37: Results showing the detection capability of IMB with 5 percent cell-to-cell variability in 10S1P string configurations

Figure 36 shows that IMB can readily detect and quantify a 20 percent aged cell in the 10S1P strings irrespective of SOC. Increasing the extent of heterogeneity (or increasing the number of

aged cells in the string) produced stronger and distinguishable signals (ΔZ′) from the baseline string, indicating the possibility of identifying the extent of heterogeneity within a string. A similar trend can be observed with 5 percent cell-to-cell variability in **Figure 37**. Thus, IMB can readily detect and quantify any heterogeneity of aging between 5 and 20 percent in a 10S1P string setting at any state of charge.

Figures 38-39 summarizes the detection capability of IMB for the parallel strings (4S1P). Unlike series string, lower SOC (e.g., 0%) weakens the detection capability of IMB. **Figure 38** shows that the difference in Z′(ΔZ′) clearly exceeds the LOQ threshold at or above 50 percent SOC when there were three 20 percent aged cell in the 4S1P string. ΔZ′ barely exceeded the LOD line but remained below the LOQ line at low frequencies when there were less than three, 20 percent aged cells in the parallel string. Reducing the extent of heterogeneity (5% aging case in **Figure 39**) slightly reduces the detection performance of IMB, but results still look promising for detection of lower levels of parallel string heterogeneity. Unlike in the series string study, the IMB was only able to detect and quantify severe cell-to-cell variability for 1S4P strings investigated in the parallel string study.

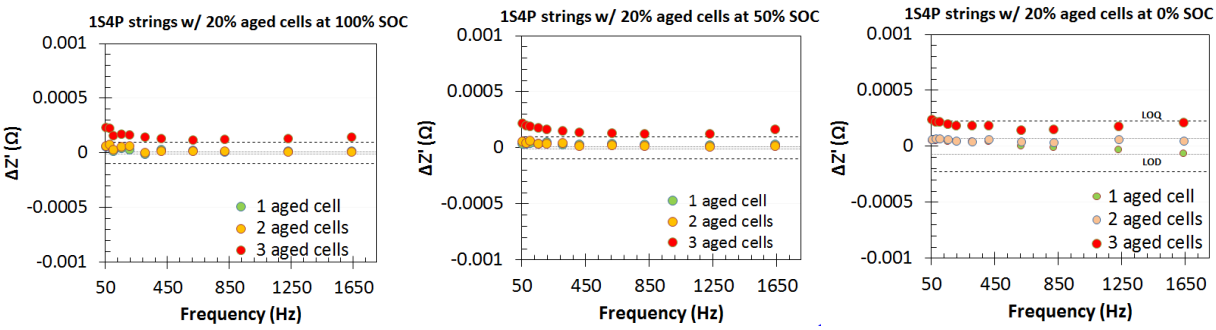

Figure 38: Results showing the detection capability of IMB with 20 percent cell-to-cell variability in 1S4P string configurations

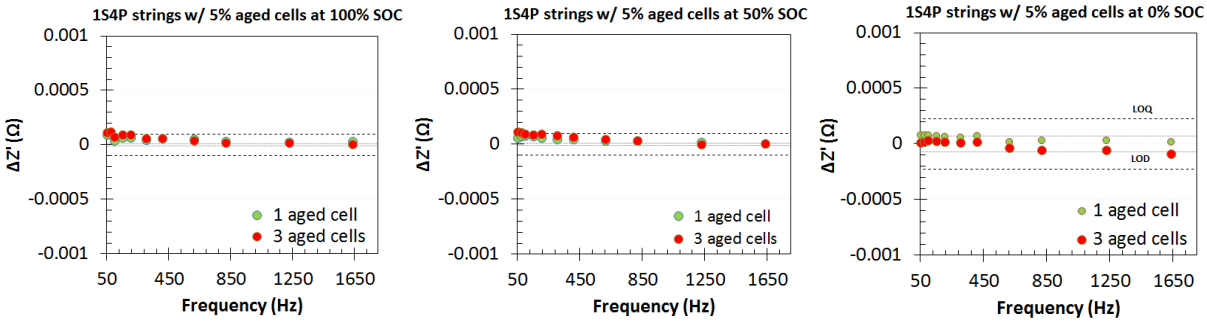

Figure 39: Results showing the detection capability of IMB with 5 percent cell-to-cell variability in 1S4P string configurations

SUMMARY

The current phase work has focused on analyzing the detection methods that have been developed as part of this project. This has included studies on NMC and LFP chemistries, as well as new studies on modules of increasing size and complexity. This effort focuses on demonstrating the applicability of the tools that have been explored as part of this project to cells and formats that are relevant to vehicle electrification; ultimately providing the background information that will be needed to successfully integrate these tools into a diagnostic or monitoring system.

Abuse testing work has focused on understanding how cell damage impacts NMC and LFP cathode chemistries, looking at both impedance analysis as well as differential capacity information that can be gleaned from cycling. Using these methods, we see strong correlation between EIS changes and increasing levels of overcharge, with trends that begin to appear at ~135 percent SOC of a NMC cell. This trend is even stronger with LFP chemistries, as there are near immediate impacts when these cells begin to overcharge.

More elevated temperatures are required to see significant impact from abusive thermal ramp tests. The trends observed were fairly subtle up to 100 °C. Above this temperature we began to see strong trends in both impedance and differential capacity data with increased temperature. The tools studied however had difficulty detecting the exposure to temperatures between 40 and 100 °C.

On the mild-abuse side, the diagnostic performance of IMB was evaluated for three in-vehicle realistic scenarios related to immediate, mid and long-term safety concerns of the battery. These evaluations were performed on automotive grade fresh and aged 16 Ah NMC pouch cells. In the first case, external shorts of varying intensities were applied to determine the detectability of various shorts. The most influential factor was the intensity of the short circuit itself, with C/5 and even C/10 shorts showing strong signals with impedance analysis, particularly immediately after application of the short circuit. The C/100 short was difficult to detect and remained only above minimum detection levels. The detection capability for shorting conditions is found to be more effective in the low-frequency range (< 5 Hz). State of charge had some impact on detection as well, with the strongest detection levels observed at 100 percent SOC, however, the more severe short circuits were generally above the minimum detection threshold at all SOC levels immediately after the short circuit was applied. Lower states of charge lost some fidelity in measurements made 10 and 30 minutes after short application. However, short circuit data suggests the ability to detect immediate safety concerns following a crash (significant aid to first responders), but as presently designed may have issues with long-term fault detection.

Detection of string imbalance found to be dependent on string size. Detection of a single cell capacity imbalance up to 20 percent in series string configurations was limited to 4S1P (four cells connected in series). Such a detection limitation on string size implies that a modular detection algorithm with IMB (at its current performance) could be implemented in larger strings.

Detection of cell-to-cell heterogeneity (or variability) in series (10S1P) and parallel (1S4P) string settings was also evaluated with impedance measurements. While IMB showed superior cell-to-cell heterogeneity detection performance for series strings, detection performance was weak for parallel strings. IMB was only able to detect and quantify severe cell-to-cell heterogeneity for the 1S4P parallel strings in the upper SOC window (>50%). Thus, going forward increased diagnostic system accuracy and resolution would be a crucial area for advancement.

FUTURE WORK

Planning is currently underway for a proposed diagnostic integration platform. The goal of this proposed work is to develop a platform for demonstrating if this and other diagnostic methods can be integrated into a full battery system. This will involve the development of the platform itself, and ultimately the testing of damaged and/or abnormal cells within a test platform in real-time to determine if a given diagnostic technique can detect a failing cell in practice.

DOT HS 812 810
January 2020

U.S. Department
of Transportation

**National Highway
Traffic Safety
Administration**

14475-100219-v2